FEB 21 2003

AFRL-SR-AR-TR-03-

0121

REPORT DOCUMENTATION PAGE

1. AGENCY USE ONLY (*Leave Blank*)	2. REPORT DATE	3. REPORT TYPE AND DATES COVERED
	27 Feb. 2003	Final, 15 Nov. 1999 - 14 Nov. 2002

4. TITLE AND SUBTITLE
Mechanisms of Hypersonic Transition on a Generic Scramjet Forebody

5. FUNDING NUMBERS
F49620-00-1-0016

6. AUTHOR(S)
Steven P. Schneider and Helen L. Reed

7. PERFORMING ORGANIZATION NAME(S) AND ADDRESS(ES)
Aerospace Sciences Laboratory, Purdue University
1375 Aviation Drive
West Lafayette, IN 47907-2015

8. PERFORMING ORGANIZATION REPORT NUMBER

9. SPONSORING/MONITORING AGENCY NAME(S) AND ADDRESS(ES)
Air Force Office of Scientific Research/NA
4015 Wilson Blvd., Room 713
Arlington, VA 22203-1954

10. SPONSORING/MONITORING AGENCY REPORT NUMBER

11. SUPPLEMENTARY NOTES

12a. DISTRIBUTION/AVAILABILITY STATEMENT
Unclassified, approved for public release.

12b. DISTRIBUTION CODE
1

13. ABSTRACT (*Maximum 200 words*)

This grant supported measurements and computations of laminar-turbulent transition on a generic scramjet forebody. The computations, described in the appendix, were carried out under a subcontract. The experiments were carried out using the new Boeing/AFOSR Mach-6 Quiet Tunnel (BAM6QT). Much of the experimental effort was expended in the first phase, completion and development of the necessary tunnel, which took longer than expected. Furthermore, although the tunnel was operational in April 2001, it is still not running quiet at significant Reynolds numbers. However, the tunnel is already successful at providing low-cost operation. The work carried out at Purdue has already been documented in a series of AIAA papers and other publications. Therefore, the present final report is a summary of past progress, current issues, and future plans.

The appendix reports mean-flow and linear-stability results. Computations are reported for Stetson's blunt cone at zero angle of attack and Mach 8 and Maslov's blunt cone at Mach 6. In addition, preliminary computations are reported for more complex geometries.

14. SUBJECT TERMS
Hypersonic laminar-turbulent transition, boundary layers, low-disturbance wind tunnels, scramjet vehicles, stability theory and computations

15. NUMBER OF PAGES
39

16. PRICE CODE

17. SECURITY CLASSIFICATION OF REPORT	18. SECURITY CLASSIFICATION OF THIS PAGE	19. SECURITY CLASSIFICATION OF ABSTRACT	20. LIMITATION OF ABSTRACT
UNCLASSIFIED	UNCLASSIFIED	UNCLASSIFIED	UNLIMITED

Final Report for AFOSR Grant F49620-00-1-0016, 15 Nov. 1999 to 14 Nov. 2002. Grant titled 'Mechanisms of Hypersonic Transition on a Generic Scramjet Forebody'

Steven P. Schneider, Associate Professor
School of Aeronautical and Astronautical Engineering
Aerospace Sciences Lab
Purdue University Airport
West Lafayette, IN 47906-3371
steves@ecn.purdue.edu, 765-494-3343

February 27, 2003

1 Summary

This grant supported measurements and computations of laminar-turbulent transition on a generic scramjet forebody. The computations, described in the appendix, were carried out under a subcontract. The experiments were carried out using the new Boeing/AFOSR Mach-6 Quiet Tunnel (BAM6QT). Much of the experimental effort was expended in the first phase, completion and development of the necessary tunnel, which took longer than expected. Furthermore, although the tunnel was operational in April 2001, it is still not running quiet at significant Reynolds numbers. However, the tunnel is already successful at providing low-cost operation, a significant accomplishment at a time when there is no operational hypersonic quiet tunnel anywhere, and little or no experimental work on hypersonic laminar instability.

The work carried out at Purdue has already been documented in a series of AIAA papers and other publications. Therefore, the present final report is a summary of past progress, current issues, and future plans. Funding for closely related work has also been provided by Sandia National Labs, NASA Langley, TRW, and NASA Johnson, so the results presented here are due in part to their support. Tunnel fabrication was supported primarily by two DURIP grants and a gift from the Boeing Company, although the labor of assembling, testing, and adapting the components was primarily supported by the present grant and by Sandia.

2 Introduction

Hypersonic laminar-turbulent transition is critical to airbreathing hypersonic cruise vehicles and reentry vehicles. The present grant supported a continuation of a 13-year effort towards obtaining repeatable measurements of the mechanisms of transition on generic shapes, as part of a cooperative effort to develop mechanism-based prediction methods.

The effect of conventional tunnel noise and the importance of quiet tunnels was reviewed and described in Refs. [13] and [17]. Conventional tunnels suffer from noise levels that are an order of magnitude higher than flight; this noise causes earlier transition, and can also change the trends in transition, so that a configuration optimized for laminar flow in a conventional tunnel might be far from optimum in flight. A review of the effect of transition on launch vehicle design was presented as Ref. [18]. In addition, reviews of the flight data for transition were presented at NASA Langley, AFRL/Hanscom, Sandia, SAIC, the Navy Strategic Systems Office, and TRW.

The author participated in NATO RTO Working Group 10, in part with support from the present grant. This work resulted in a review of instability and transition on round cones. Laminar-instability data near zero angle of attack was reviewed in Ref. [19], while Ref. [22] emphasized bluntness and angle-of-attack effects. A NATO RTO document is expected to appear based on the results of this working group. A NATO RTO working group focusing on hypersonic transition was proposed, but the Exploratory Team investigating the proposal found insufficient European interest.

3 Results

3.1 Laser-Perturbation Experiments

Earlier measurements carried out in the Mach-4 tunnel under previous AFOSR grants have now appeared as journal articles [8, 9]. The laser perturbation method is now being considered by Roger Kimmel of AFRL for use as an acoustic perturbation method in the BAM6QT. To enable this, a 2-inch conformal window was fabricated for the BAM6QT by Metrolaser, with support from AEDC and AFRL, and with technical assistance from Purdue.

3.2 Laser-Differential Interferometer Measurements on Blunt Nose

Work on a laser differential interferometer (LDI) was also initiated under a past AFOSR grant. Experiments were carried out using the LDI for repeatable measurements of the response of a blunt-nose flowfield to a localized laser-induced perturbation. These experiments were continued and completed while the student was supported by other funds [6, 7]. The results promise to form a database for development and validation of time-resolved computations for receptivity effects. They also shed light on the blunt-body paradox.

3.3 Development of the 9.5-inch Mach-6 High Reynolds Number Quiet Ludwieg Tube

The first phase of the research proposed in 1999 was the completion and shakedown of this tunnel; in the end this phase consumed the majority of our efforts during 1999-2002.

The tunnel is the result of development work that began in 1990. A Mach-4 Ludwieg tube was constructed at Purdue in 1992, using a 4-inch nozzle of conventional design that was obtained surplus from NASA Langley. By early 1994, quiet-flow operation was demonstrated at the low Reynolds number of about 400,000 [10]. Since then, this facility has been used for development of instrumentation and for measurements of instability waves under quiet-flow conditions (e.g., Ref. [20, 8, 5]). However, the low quiet Reynolds number imposes severe limitations; for example, the growth of instability waves under controlled conditions on a cone at angle of attack was only about a factor of 2 [3]. This is far smaller than the factor of $e^9 - e^{11}$ typically observed prior to transition, and small enough to make quantitative comparisons to computations very difficult.

A facility that remains quiet to higher Reynolds numbers was therefore needed. The low operating costs of the Mach-4 tunnel had to be maintained. However, hypersonic operation was needed in order to provide experiments relevant to the hypersonic transition problems described earlier. Operation at Mach 6 was selected, since this is high enough for the hypersonic 2nd-mode instability to be dominant under cold-wall conditions, and high enough to observe hypersonic roughness-insensitivity effects, yet low enough that the required stagnation temperatures do not add dramatically to cost and difficulty of operation. Reference [12] describes the overall design of the facility, and the detailed aerodynamic design of the quiet-flow nozzle, carried out using the e^N method. A version of this paper recently appeared in journal form [16]. A detailed aerodynamic design of the contraction was also carried out [11]. Reference [11] also supplies a preliminary report on the detailed mechanical design of the nozzle and contraction. Reference [14] reported on design and testing of some of the component parts, including the driver-tube heating, the as-measured contraction contour, the throat-region mandrel fabrication and polishing experience, and so on. This reference was the first reported during the present grant.

Ref. [15] reports on the design and fabrication of the support structure, diffuser, and second-throat section (which also serves as the sting support). It also reports experience with final contraction fabrication, and with operation of the vacuum system. Ref. [15] also reports on the contour measurements on the third attempt at throat-mandrel fabrication, which completed polishing with good success. Ref. [23] reports (1) the nozzle fabrication, including some of the wall-contour measurements, (2) the contraction-region heating apparatus, (3) the burst-diaphragm tests, (4) the bleed-slot suction system, (5) the electroformed throat properties, and (6) initial hot-wire calibrations.

Ref. [24] reports the rest of the measurements of the as-fabricated nozzle, including initial measurements of tunnel performance. The mean flow and fluctuations were measured in the centerplane using fast pressure transducers (cp. Ref. [10]). Ref. [25] reported on progress in tunnel shakedown and instrumentation development, including efforts to achieve the desired

quiet flow by modifying the geometry of the bleed-slot throat, and initial attempts to measure the stagnation temperature in the flow using cold wires. Ref. [2] reported the stress-analysis and testing of the initial conformal window, fabricated in 2001. The present tunnel name was adopted in Spring 2001. Ref. [21] reported initial hot-wire measurements, the effect of driver-tube temperature on tunnel noise, blockage test results, and the effects on quiet flow of nozzle temperature distribution and bleed-slot throat geometry. Ref. [22] reported on the seventh bleed-slot throat geometry, the effect of polishing the downstream portions of the nozzle, pitot measurements on the centerline forward, and the effect of downstream model-mount and diffuser conditions on measurements in the nozzle.

The tunnel is not yet quiet, except perhaps at low Reynolds numbers, where at present the nozzle-wall boundary layers appear separated. This disappointment must be set against the difficulty of hypersonic laminar flow control. There is no operational hypersonic quiet tunnel anywhere in the world at present.

The tunnel *is* successfully operating reliably at low cost for useful runtimes. The core flow is uniform, the polished throat remains clean, and large models have been successfully started. Hot-wire and temperature-sensitive paints techniques have been successfully developed to measure traveling and stationary wave growth. Although much remains to be done, and progress is slower than initially planned, no show-stoppers are evident. The current path remains the lowest-cost approach to obtaining detailed measurements of the mechanisms of transition under low-noise conditions comparable to flight.

The only alternative on the horizon would be measurements in a reinstalled NASA Langley Mach-6 quiet nozzle; while this would be desirable, the full operational costs of this facility would greatly exceed those of the BAM6QT, due to the long run-time and large air supply. Furthermore, development of the BAM6QT remains the obvious next step in the development of more capable hypersonic quiet tunnels. Development of the BAM6QT and instrumentation should continue unless a show-stopper or a better alternative is found.

3.4 Measurements on Generic Scramjet Forebodies

Earlier measurements on an axisymmetric forebody appeared in journal form as Ref. [1].

The Hyper2000 geometry is very similar to the Hyper-X. A model was fabricated at Purdue in 2001-2002 using this geometry. The role of streamwise vortices in transition was studied, beginning with initial results reported in Ref. [21]. The measurements were carried out using temperature sensitive paints, with roughness elements on the leading edge using as controlled perturbers [22]. The vortices are most easily generated using roughness at the leading edge, although vortex growth is small until the first compression corner is reached. The effect of roughness height and spacing is being studied, along with the effect of Reynolds number, with the final results to appear in AIAA papers in summer 2003, and in Shin Matsumura's M.S. thesis.

3.5 Computational Work at Arizona State University

Approximately one third of the present grant supported cooperative computations by Prof. Helen Reed's group at Arizona State University. This work was recently summarized in Ref. [4]. In additiona, a final report for the subcontract is appended.

4 Current Status and Future Plans

Work on hypersonic laminar-turbulent transition continues, with continuing support from AFOSR, Sandia, and NASA. AFOSR-funded efforts are now focused primarily toward achieving quiet flow. Craig Skoch's Ph.D. thesis work will focus on this topic until quiet flow is achieved. Our current effort is aimed at diffuser and model-mount effects, upstream pitot measurements, and improved leak detection.

Erick Swanson recently finished an M.S. thesis performing temperature-sensitive paint measurements on round cones at angle of attack, looking for crossflow vortices. He will shift to partial AFOSR support, and continue to look at crossflow and roughness induced transition on blunt cones at angle of attack.

Shann Rufer's Ph.D. thesis will be on hot-wire measurements of instability waves on blunt cones at zero and non-zero angle of attack. She has been supported by Sandia. Plans include measurements with controlled perturbations from a glow apparatus. Uncalibrated measurements have already been obtained on a cone at Mach 6.

Shin Matsumura performed the temperature-paints measurements on the Hyper2000, and plans outside employment after his M.S. thesis in summer 2003. He has been supported primarily by NASA Langley. Additional work on the Hyper2000 will depend on tunnel progress and future funding.

5 Acknowledgements

Portions of the work were also supported by Sandia National Laboratory, under contracts BG-7114 and 80377, by NASA Langley, under grants NAG1-01-027 and NAG1-02047, by NASA Johnson, under grant NAG9-1385, and by a fellowship from TRW. The tunnel fabrication was supported by DURIP grants F49620-98-1-0284 and F49620-99-1-0278, and a gift from the Boeing Company. AFOSR support has also continued, under grant F49620-03-1-0030. The work of the authors cited is complemented by the craftsmanship of the Purdue Aeronautics Shop. The work has also benefited from continued advice from Steve Wilkinson, James Kendall, and others.

References

[1] Takeshi Ito, Laura A. Randall, and Steven P. Schneider. Effect of noise on roughness-induced boundary-layer transition for scramjet inlet. *J. Spacecraft and Rockets*, 38(5):692–

698, September-October 2001.

[2] S.W. Kwon and Steven P. Schneider. Stress analysis for the window of the Purdue Mach-6 quiet-flow Ludwieg tube. Paper 2002-0309, AIAA, January 2002.

[3] Dale W. Ladoon and Steven P. Schneider. Measurements of controlled wave packets at Mach 4 on a cone at angle of attack. Paper 98-0436, AIAA, January 1998.

[4] H. Reed, W. Saric, I. Lyttle, and Y. Asada. Stability and control of high-speed flows. Paper 2001-2700, AIAA, June 2001.

[5] Terry R. Salyer, Steven H. Collicott, and Steven P. Schneider. Feedback stabilized laser differential interferometry for supersonic blunt body receptivity experiments. Paper 2000-0416, AIAA, January 2000.

[6] Terry R. Salyer, Steven H. Collicott, and Steven P. Schneider. A laser generated thermal spot model for accurate CFD receptivity simulations. Paper 2002-3230, AIAA, June 2002.

[7] Terry Ray Salyer. *Laser differential interferometry for supersonic blunt body receptivity experiments.* PhD thesis, School of Aeronautics and Astronautics, Purdue University, May 2002.

[8] J.D. Schmisseur, Steven H. Collicott, and Steven P. Schneider. Laser-generated localized freestream perturbations in supersonic and hypersonic flows. *AIAA Journal*, 38(4):666–671, April 2000.

[9] J.D. Schmisseur, Steven P. Schneider, and Steven H. Collicott. Supersonic boundary-layer response to optically generated freestream disturbances. *Experiments in Fluids*, 33(2):225–232, August 2002.

[10] S. P. Schneider and C. E. Haven. Quiet-flow Ludwieg tube for high-speed transition research. *AIAA Journal*, 33(4):688–693, April 1995.

[11] Steven P. Schneider. Design and fabrication of a 9-inch Mach-6 quiet-flow Ludwieg tube. Paper 98-2511, AIAA, June 1998.

[12] Steven P. Schneider. Design of a Mach-6 quiet-flow wind-tunnel nozzle using the e**N method for transition estimation. Paper 98-0547, AIAA, January 1998.

[13] Steven P. Schneider. Effects of high-speed tunnel noise on laminar-turbulent transition. Paper 2000-2205, AIAA, June 2000.

[14] Steven P. Schneider. Fabrication and testing of the Purdue Mach-6 quiet-flow Ludwieg tube. Paper 2000-0295, AIAA, January 2000.

[15] Steven P. Schneider. Initial shakedown of the Purdue Mach-6 quiet-flow Ludwieg tube. Paper 2000-2592, AIAA, June 2000.

[16] Steven P. Schneider. Laminar-flow design for a Mach-6 quiet-flow wind tunnel nozzle. *Current Science*, 79(6):790–799, 25 September 2000.

[17] Steven P. Schneider. Effects of high-speed tunnel noise on laminar-turbulent transition. *Journal of Spacecraft and Rockets*, 38(3):323–333, May–June 2001.

[18] Steven P. Schneider. Hypersonic boundary-layer transition research for scramjet forebody design, October 2001. Presented at the 13th Annual Symposium of the Propulsion Engineering Research Center, NASA Marshall Space Flight Center.

[19] Steven P. Schneider. Hypersonic laminar instability on round cones near zero angle of attack. Paper 2001-0206, AIAA, January 2001.

[20] Steven P. Schneider, Steven H. Collicott, J.D. Schmisseur, Dale Ladoon, Laura A. Randall, Scott E. Munro, and T.R. Salyer. Laminar-turbulent transition research in the Purdue Mach-4 quiet-flow Ludwieg tube. Paper 96-2191, AIAA, June 1996.

[21] Steven P. Schneider, Shin Matsumura, Shann Rufer, Craig Skoch, and Erick Swanson. Progress in the operation of the Boeing/AFOSR Mach-6 quiet tunnel. Paper 2002-3033, AIAA, June 2002.

[22] Steven P. Schneider, Shin Matsumura, Shann Rufer, Craig Skoch, and Erick Swanson. Hypersonic stability and transition experiments on blunt cones and a generic scramjet forebody. Paper 2003-1130, AIAA, January 2003.

[23] Steven P. Schneider, Shann Rufer, Laura Randall, and Craig Skoch. Shakedown of the Purdue Mach-6 quiet-flow Ludwieg tube. Paper 2001-0457, AIAA, January 2001.

[24] Steven P. Schneider and Craig Skoch. Mean flow and noise measurements in the Purdue Mach-6 quiet-flow Ludwieg tube. Paper 2001-2778, AIAA, June 2001.

[25] Steven P. Schneider, Craig Skoch, Shann Rufer, Shin Matsumura, and Erick Swanson. Transition research in the Boeing/AFOSR Mach-6 quiet tunnel. Paper 2002-0302, AIAA, January 2002.

Appendix: Report on Computational Work

Final Report for Computational Subcontract under AFOSR Grant F49620-00-1-0016
15 Nov. 1999 to 14 Nov. 2002
Mechanisms of Hypersonic Transition on a Generic Scramjet Forebody

Helen L. Reed, Professor
Mechanical & Aerospace Engineering
Arizona State University
Tempe, Arizona 85287-6106

1 Summary

This grant supported measurements and computations of laminar-turbulent transition on a generic scramjet forebody. The computations were conducted at Arizona State University under subcontract from Purdue. The present final report is a summary of past progress and future plans. Funding for closely related work has also been provided by Sandia National Labs. Computer resources were available through the Sandia effort.

2 Introduction

2.1 Computational Approach

To reach high quiet Reynolds numbers, a new Mach-6 quiet-flow Ludwieg tube is being developed. Mach 6 is high enough to permit 2nd-mode dominated transition and hypersonic roughness effects, but low enough to keep heating-related instrumentation and facility costs to a minimum. Mean flow and disturbance measurements are to be carried out on the generic geometry at Purdue, and compared to computational results generated at ASU.

Our computational work focuses on two geometries: (1) The spherically-blunted round cone at zero angle of attack, for verification and validation, (2) The centerline of the Hyper2000 forebody including the compression corners, for validation. Specifically, we have revisited the Stetson experimental case at Mach 8 for verification of our codes. Then we are studying the second mode instability at Mach 6 under ideal-gas conditions, modelling both the Schneider and Maslov blunt-cone experiments for validation. For AFOSR we are simultaneously studying the Hyper2000 forebody under Mach-6 ideal-gas conditions. To then extend the computations for the Hyper2000 to hot hypersonic conditions, including non-equilibrium chemistry, we are first studying the theater-missile-defense model of Johnson & Candler at Mach 13.6 (AIAA 97-0554) for code verification.

3 Results

3.1 Cone

Using a finite-volume code, the Navier-Stokes equations are solved for a series of flows around spherically-blunted cones. These solutions are used to initially perform linear-stability analyses

to determine the growth of second-mode disturbances. (Nonlinear parabolized stability equation analyses are to follow.) Two cases are investigated: the Stetson experiment, and a recent experiment conducted at the Institute of Theoretical and Applied Mathematics in Russia. Comparisons are made with both basic-state and disturbance-state quantities. For both cases, linear-growth regions are identified. For the Stetson case, using an experimentally determined wall-temperature distribution for the basic-state appears to give better agreement with the experimentally measured growth than does the classical adiabatic-wall boundary-condition. For the ITAM case, initial comparisons are made and we anticipate continuing a careful collaboration.

3.1.1 Introduction

The central assumption of linear stability theory (LST) is that the disturbance amplitudes are small enough that disturbance interactions (either with other disturbances or with the basic state) are small enough that they may be neglected. The behavior of a disturbance is independent of its amplitude. One of the principal assumptions of LST is that the basic-state flow is locally parallel. This means that there is a streamwise direction, in which the flow is approximately constant. It is important that flow gradients in the streamwise direction be much smaller than flow gradients in the body-normal direction. For the flows considered in this report, the parallel assumption is valid.

Given a parallel flow, one chooses a body-normal direction y, a streamwise direction x, and an azimuthal/spanwise direction z. The disturbance state is a linear superposition of normal modes, each of which has the following form.

$$Q'(t,x,y,z) = Q(y)\, e^{i(\alpha x+\beta z-\omega t)} + C.C. \qquad (1)$$

Here, $Q(y)$ is the amplitude function, α is the wavenumber in the streamwise direction, β is the wavenumber in the azimuthal direction, and ω is the frequency. Each of these quantities is potentially complex-valued. If the temporal stability is considered, α is taken as real-valued. A disturbance of a certain wavelength is investigated. A linear eigenvalue problem results; the imaginary part of ω determines the growth or decay of the disturbance. If the spatial stability is considered, ω is taken as real-valued. A disturbance of a certain frequency is investigated. A non-linear eigenvalue problem, in α and α^2, results; with the imaginary part of α determining the growth or decay of the disturbance.

Disturbances within compressible boundary-layers are termed first-mode or second-mode. First mode instabilities are also known as inviscid instabilities. Lees and Lin (1946) show that a sufficient condition for the existence of an inviscid instability is the presence of a generalized inflection point, defined as follows.

$$\frac{\partial}{\partial y}\left(\rho\frac{\partial u}{\partial y}\right) = 0 \qquad (2)$$

Hudson et al. (1997) describe the first mode as a vortical mode and point out that the generalized inflection point indicates a maximum in the angular momentum. The second mode is particular to compressible boundary layers, and is sometimes referred to as an acoustic mode. In his review work, Mack (1984) discusses the physics of these disturbances. One important result is that the second-mode wavelength is tuned to the thickness of the boundary layer. This second mode,

which emerges for flows where a characteristic Mach number is greater than 4, is recognized as the most unstable disturbance for high-speed flows. This is confirmed by a series of experiments, including the work of Kendall (1975), Demetriades (1977), and Stetson et al. (1984). The first mode is distinguished from the second mode by using a local Mach number. This Mach number is the difference between the phase velocity of the disturbance (c_r) and the basic state velocity (u), divided by the local sonic speed (a).

$$\tilde{M} = \frac{c_r - u}{a} \tag{3}$$

If $\tilde{M}^2 < 1$ everywhere within the boundary layer, then the first mode may be present. If $\tilde{M}^2 > 1$ somewhere within the boundary layer, the flow is unstable to "Mack" modes, the most unstable of which is the second mode.

As Schneider (2001b) points out, accurate depiction of the growth of a second-mode instability wave over a circular cone at zero-angle of attack remains a challenge, both computationally and experimentally. Despite the acknowledged limitations of linear stability theory, it can still be of considerable use towards attaining this goal.

Experiments can be conducted to identify linear-growth regions; computations can be used to investigate more of the details. The series of experiments performed by Stetson et al. (1984), who consider the growth of instabilities on right-circular cones (both sharp and blunted) at zero-angle-of- attack at Mach 8, serves as a benchmark for subsequent computations. Numerical comparisons to the observed growth of second-mode instabilities over the spherically blunted-cone are reported by Malik et al. (1990), Esfahanian (1991), Kufner et al. (1993), and Rosenbloom et al. (1999). Agreement with the experimentally observed growth rates can be described as qualitative.

Schneider (2001b) discusses these comparisons in some detail. He concludes that one of the major difficulties with these comparisons lies with the signal-to-noise ratio found in the stability measurements of the Stetson experiment. This speaks to the immense challenges faced by experimentalists in this field. The signal-to-noise ratio presents problems because discernible growth of the second mode in the experiment takes place where there is a noticeable presence of a higher harmonic - suggesting that nonlinearities are present.

To address this problem, a new set of low-enthalpy high-speed experiments is carried out for spherically-blunted cones, at Purdue University, by Prof. Steven Schneider, and at the Institute of Theoretical and Applied Mathematics (ITAM, in Novosibirsk, Russia), by Dr. Alexander Shiplyuk (Maslov 2001). The goal of this set of experiments is to measure the growth of second-mode disturbances over circular cones in a low-noise environment (Maslov 2001). Consistent with previous experiments, Maslov (2001) finds two-dimensional second-mode disturbances to be the most unstable.

For flows where the linear growth of disturbances is a part of the path to transition, a sensible way to delay transition is to modify the flow such that the linear growth of disturbances is lowered. For high-speed flows, Kimmel (2003) reviews recent activity in this area, which includes wall-cooling, leading-edge modification, and passive porosity. Of these methods, passive porosity is studied actively by a research community that includes the ITAM group in

Novosibirsk, Russia. The central idea of this technique is to exploit the acoustic nature of second-mode disturbances by changing the acoustic impedance of the wall (Kimmel 2003). Federov et al. (2003) report the stabilization of second-mode disturbances, both numerically and experimentally, by replacing a solid surface with an ultrasonically absorptive coating, in this case, a porous metal felt. Better understanding of the second-mode disturbances, achieved through careful and deliberate collaboration between experiment and theory, is an important step to fully exploiting transition-delaying techniques.

In this report, two cases are investigated. The first is a revisiting of the classical Stetson et al. (1984) experiment. The second is an investigation of a recent experiment conducted at ITAM. Both cases concern spherically-blunted right-circular cones at zero-incidence. Both cases involve supersonic freestream flows such that two-dimensional second-mode instabilities are dominant. In both cases, the experimentally determined growth of second-mode disturbances is compared with numerical predictions made using LST.

3.1.2 Numerical Methods

Two steps are used to obtain a stability estimate for a given flow. The first is to determine the steady, mean-flow solution, the basic-state. The second step is to solve a set of disturbance equations. In this report, linear-stability theory is used.

Basic-State Solution Method

The basic-state equations are the full Navier-Stokes equations, solved using a calorically perfect gas model and the Sutherland Law for viscosity and thermal conductivity. The equations are cast in a cylindrical coordinate system to exploit the axi-symmetry of the problems.

The physical space is discretized into a structured collection of finite-volumes. Because parallel computers are used, the computational domain is divided into a series of normal-to-wall strips. A typical grid arrangement is shown in Figure 1. The overlap regions shown are those cells for which "neighboring" processors share information.

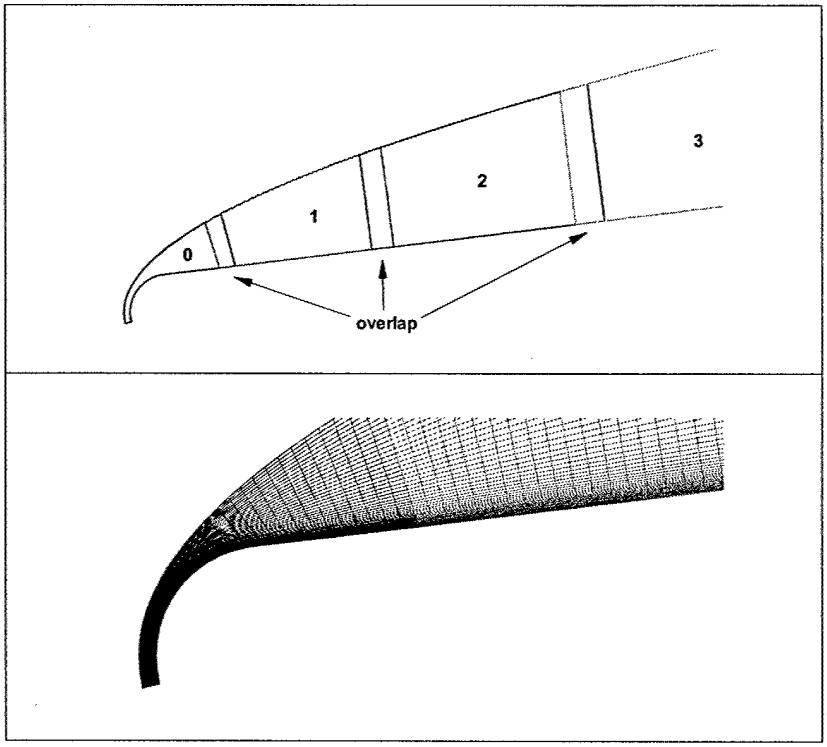

Figure 1: Distibution of cells among processors in physical-space.

The inviscid fluxes are determined using a second-order-accurate finite-volume approach. Because shock-fitting is used to fix the outer boundary, limiting is not necessary for the inviscid fluxes outside of the stagnation-line region. The viscous fluxes are determined using second-order accurate finite-differences. The boundary conditions are very standard. At the stagnation line, symmetry is used. At the outflow, extrapolation is used. At the wall, no-slip and zero-normal pressure-gradient conditions are imposed. Either adiabatic-wall or temperature-specified wall can be modeled. As mentioned above, shock-fitting is used for the outer boundary. The Rankine-Hugoniot jump-conditions are satisfied, while characteristic information from the interior is used as a numerical boundary condition to complete the system.

To solve the set of implicit equations, the Data-Parallel Line-Relaxation (DPLR) method (Wright et al., 1996) is used. To summarize this method, the two limiting cases of explicit integration and implicit integration are discussed. Explicit integration provides two benefits: each time-step integration is relatively inexpensive, and there is a certain data independence that lends itself to parallelization. Implicit integration allows for much larger time steps, hence fewer time steps to convergence. However, each time step is more computationally expensive due to the evaluation of the linearizations and the solution of the implicit system of equations. As well, the inversion of the nine-point block-stencil system is prohibitive, and does not lend itself to parallelization.

Wright et al. (1996) recognize that for a class of flows, similar to the ones studied here, the gradients in the wall-normal direction are generally much larger than those in the streamwise direction. This same observation is made for the thin-layer Navier-Stokes formulation. The

supposition made by Wright et al. (1996) is that the equations are stiffer in the normal direction than they are in the streamwise direction. The details of the DPLR method are comprehensively presented by Wright et al. (1996). A brief summary is presented here.

The fully implicit system, written for a given cell indexed (i, j), can be written as follows.

$$\sum_{I=-1}^{1}\sum_{J=-1}^{1} A_{i,j,I,J}\,\Delta Q_{i+I,j+J} = RHS_{i,j} \tag{4}$$

The term $RHSi,j$ is a vector representing the right-hand-side. The term $A_{i,j,I,J}$ is a matrix which contains the appropriate linearization. The term $\Delta Q_{i+I,j+J}$ is a vector representing the change in the solution. What Wright et al. (1996) propose is that an iterative loop (k) be established within a given time step.

$$\sum_{J=-1}^{1} A_{i,j,0,J}\,\Delta Q^{k+1}_{i,j+J} = RHS_{i,j} - \sum_{J=-1}^{1} A_{i,j,-1,J}\,\Delta Q^{k}_{i-1,j+J} - \sum_{J=-1}^{1} A_{i,j,1,J}\,\Delta Q^{k}_{i+1,j+J} \tag{5}$$

In effect, the streamwise linearizations are lagged. What remains on the left-hand side is a block tri-diagonal system of equations. A LU-decomposition is made of the system on the first iteration, which speeds up the solution of subsequent iterations. The first iteration, at ($t = 0$) is executed using a CFL number of 0.5, and setting ΔQ^0 to zero. Following each iteration, the data are communicated between neighboring processes using MPI libraries (Message Passing Interface Forum 1995). For subsequent time steps, ΔQ^0 is set to the converged ΔQ value from the previous time step. The CFL number is gradually increased until the numerical stability of the solution is reached. As well, the solution procedure is stabilized using under-relaxation.

Linear Stability Solution Method

The fundamental principle of linear stability theory is that a small disturbance is assumed in a steady, "parallel" flow. Such a disturbance is also assumed to have a wave-like structure in time and two spatial directions. To determine the disturbance equations, the Navier-Stokes equations are linearized. The first term in a Taylor series is kept, and higher-order-terms are dropped. The disturbance flow is assumed to have the form shown in Equation (1), with a given frequency and wavenumber. The resulting derivatives in the normal direction are evaluated using fourth-order accurate differences. All the disturbances investigated in this report are two-dimensional, $\beta = 0$.

The boundary conditions used are identical to those used in the basic-state solution, with one exception. The frequencies of the disturbances investigated are high enough that the thermal capacity of a typical wall surface is high enough that no temperature disturbance can be supported, thus $T' = 0$ at the wall. An eigenvalue problem results, where A, B, C, D are block-pentadiagonal matrices and x is the disturbance eigenvector.

$$\left(A + \omega B + \alpha C + \alpha^2 D\right)x = 0 \tag{6}$$

In terms of the stability problem, either temporal stability (α known, ω found) or spatial stability (ω known, α found) is considered. Regardless of which problem is considered, one can use either a global approach or a local approach. In the global approach, all (or many) eigenvalues are found. In the local approach, only a few eigenvalues – in the neighborhood of a guess – are found. ARPACK (Lehoucq et al. 1998) is used to find the particular eigenvalues. For the spatial stability problem, the spatial problem is converted from quadratic to linear. If the temporal

problem uses 5 × 5 matrices for each of the blocks, this approach to the spatial problem uses 10 × 10 matrices for each of the blocks.

Upon initial investigation of a case, the global method is used to find a large number of eigenvalues in the suspected vicinity of a physical eigenvalue. This procedure is used for two different cases, e.g. a 500 × 150 case and a 500 × 300 case. The physical eigenvalues remain constant (within some convergence tolerance), while the spurious eigenvalues are different for each case. Once a physical eigenvalue is identified, the more-efficient local method is used.

3.1.3 Stetson Case

The Stetson et al. (1984) geometry is a 7° half-angle right-circular cone, with a blunted nose of radius 3.81 mm. The total length of the model is just over 1 m (*s = 267*). The free-stream flow is Mach 8, with zero-incidence with respect to the cone's axis. The Reynolds number (based upon free-stream conditions and the nose radius) is 3.3×10^5. The focus of the experiment is the second-mode instability, which is thought to be dominant for high-speed flows over smooth, convex, axi-symmetric geometries in two-dimensional flow.

Schneider (2001b) summarizes the Stetson experimental conditions very efficiently. Paraphrasing Schneider, the total pressure is 4.00 MPa; the total temperature is 750 K. On the cone, surface measurements are taken for pressure and temperature. Basic-state profiles are measured using total-temperature and pitot-pressure probes. Basic-state comparisons between experimentally determined profiles and computed profiles are discussed below. For the Stetson experiment, disturbances are measured using a series of four hot-wire anemometers. Starting at 0.254 m (s = 66:7), disturbance spectra are measured through 0.922 m (s = 242). The measured total-temperature spectra are shown in Figure 2; it bears repeating that $\omega = 1$ corresponds to $f^* =$ 49.5 kHz. The second-mode disturbances correspond to the spectral peaks that appear in the range $2.5 < \omega < 3$.

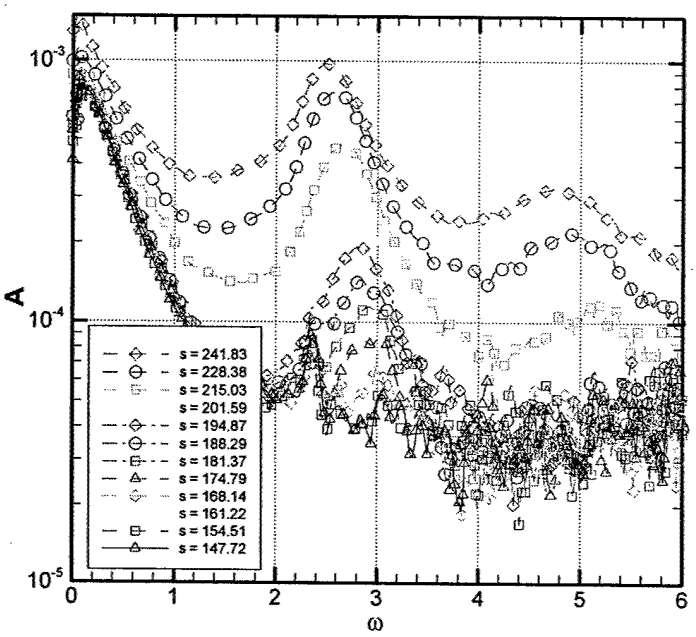

Figure 2: Stetson experiment: measured disturbance spectra of total temperature

From Figure 2, there follow some observations about the experiment. Firstly, Schneider (2001b) notes that the experimental (free-stream) environment is not quiet, thus Figure 2 shows the growth of broadband, uncontrolled disturbances that result from the free-stream noise. Secondly, one notices the presence of a harmonic of the second-mode disturbance, starting at s = 215. This implies that non-linear interactions may be important downstream of s = 215. Summing up, the validity of comparing these experimental results with linear stability theory is limited by the free-stream disturbance environment and the possible presence of non-linear interactions.

Following Malik et al. (1990), many numerical investigators have chosen s = 175 as the place to make a comparison with the second-mode growth-rates reported by Stetson. As seen in Figure 3, the numerically determined growth rates (including ours) consistently peak roughly 60% higher than the peak growth-rate reported by Stetson. According to Schneider (2001b), Stetson cites the non-negligible growth rates of second-harmonics of second-mode waves at s = 175 as evidence of non-linearity. Stetson believes this is the reason for the disjoint between linear-stability theory and the experimentally reported growth rates.

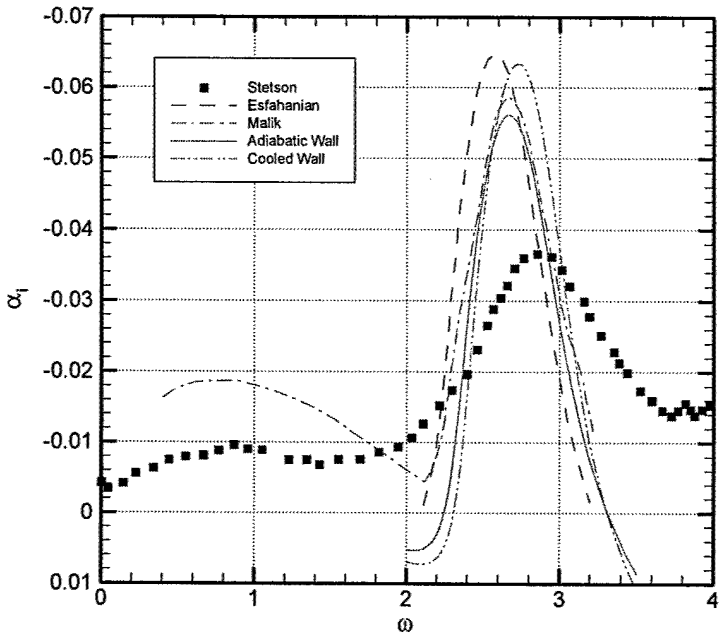

Figure 3: Second-mode growth rates as functions of frequency at s=175.

Schneider (2001b) investigates this idea further, obtaining the raw data from the Stetson experiment (and also kindly providing it to us). Part of this data is shown in Figure 2. Discussing this data, Schneider proposes that there exists a small linear-growth region. This region would begin at s = 195, the furthest-upstream location where the amplified frequencies are clearly delineated from the noise. The region would end at s = 215, where there appear second-harmonic waves with significant amplitude.

To investigate this theory, Schneider (2001b) combines linear-stability theory results from Rosenbloom et al. (1999) and those of Stetson et al. (1984) (using data from Figure 2) to form Figure 4. In this figure, the amplitudes of the disturbances are normalized by their values at s = 195. The logarithm of the amplitude ratio is the N-factor. Comparing the numerical and experimental N-factors in the range $195 < s < 215$, there appears much better qualitative agreement between theory and experiment than appears in Figure 3 at s = 175.

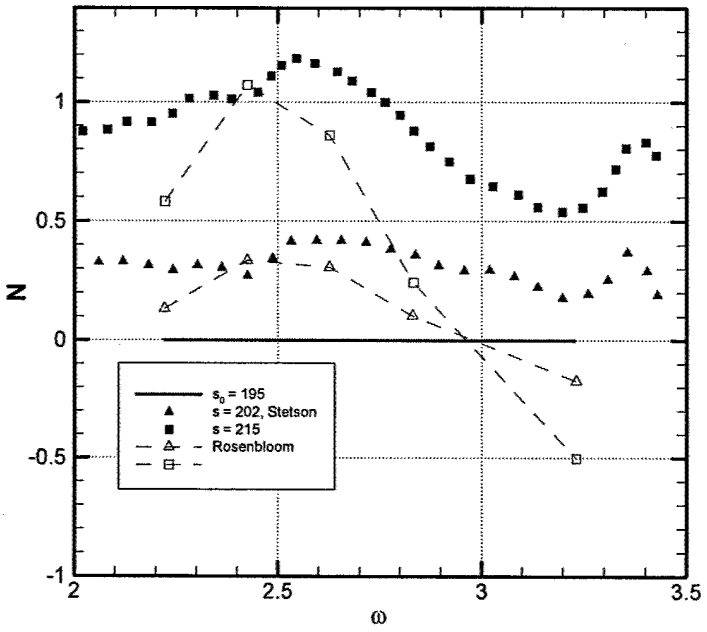

Figure 4: Comparison of Stetson N-factors with Rosenbloom, $s_0 = 195$.

Computational Parameters

The flow conditions are summarized in Table 1. The flow is modeled as an ideal gas with $\gamma = 1.4$ and a constant Prandtl number of 0.72. The surface is modeled as adiabatic. Three cases are run on parallel computers. For these cases, the domain in the streamwise direction is truncated at s = 250. The mesh sizes for these cases are 500×150 and 500×300, and 1000×150.

Variable	Normalization	Value
s, δ	r^*	3.810×10^{-3} m
ρ	ρ_∞^*	2.627×10^{-2} kg/m^3
u	U_∞^*	1.185×10^{3} m/s
p	p_∞^*	4.124×10^{2} Pa
T	T_∞^*	5.447×10^{1} K
ω	U_∞^* / r^*	3.110×10^{5} rad./s
α	$1/r^*$	2.625×10^{2} rad./m

Table 1: Non-dimensionalizations used for Stetson case.

Basic-State Results

Verification The verification of the basic-state results includes two steps. The first is an internal check of the grid-independence of the solution. The second step is a comparison with other results, principally those of Esfahanian (1991) and Stetson et al. (1984).

In order to estimate the truncation error in the basic-state solution, the surface temperatures at $s = 175$ are compared for the three meshes used. This does not represent the maximum error in the solution. Instead, it represents the level of truncation error in an interesting region of the solution. From Table 2, it is evident that the adiabatic surface temperatures are in agreement, among all three meshes. It is also noticed that doubling the mesh in the streamwise direction affects the convergence less than does doubling the mesh in the normal direction. At any rate, the truncation error for the 500×150 case, at $s = 175$, can be described as being of $O(10^{-4})$. The normalized deviations, used to estimate the truncation error, are calculated as follows.

$$Norm.\ Dev. \equiv \left| \frac{b-a}{a} \right| \tag{7}$$

Grid	Temperature	Normalized Deviation
500 × 150	11.864823	-
1000 × 150	11.864576	2.08×10^{-5}
500 × 300	11.864030	6.68×10^{-5}

Table 2: Comparison for surface temperature at s = 175.

In comparing the results with those of Esfahanian (1991), it is notable that the code written in support of this report is a finite-volume, shock-fitting, full Navier-Stokes (NS) solver. The code written by Esfahanian (1991) is a finite-difference, shock-fitting, thin-layer Navier-Stokes (TLNS) solver. The mesh size used by Esfahanian (1991) is 1300×200. The treatment of viscous terms distinguishes a TLNS solver from an NS solver. Whereas an NS solver includes all the viscous terms, a TLNS solver drops viscous derivatives in the streamwise direction. This is based on the assumption that derivatives in the streamwise direction are much smaller than those in the normal direction. For the flow under consideration, this is a valid assumption far from the blunted nose. Keeping this in mind, one should expect good agreement between the two solutions at a location downstream. Any disagreements are expected to be found in the nose region.

In Figure 5, surface-temperature distributions are compared, showing the entire domain. The values obtained using the current method are compared with those found by Esfahanian (1991). It is evident that the farther from the nose one considers, the better the solutions agree. It is thought that the disagreement in the nose region, particularly at the sphere-cone interface, is due to the assumptions made to use the TLNS formulation. As noted above, the principal assumption of TLNS is that the viscous derivatives in the streamwise direction are small compared to the viscous derivatives in the body-normal direction. Although generally a valid assumption, it would be expected that the validity would suffer in the nose region.

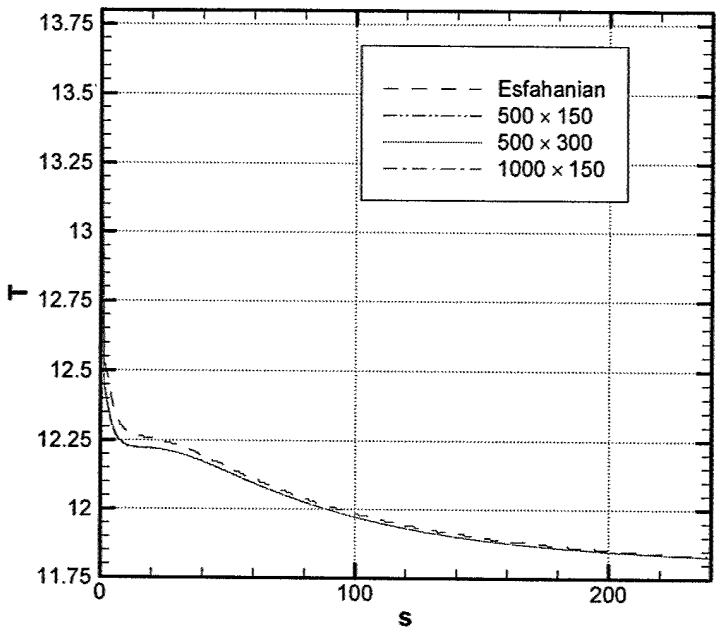

Figure 5: Comparison of surface-temperature profiles, Stetson case.

To verify the current solutions in the body-normal direction, a series of profiles are compared at the streamwise locations $s = 175$ and $s = 128$. In Figure 6 and Figure 7, streamwise velocity profiles are compared, showing the classical boundary-layer profile. Comparing the solutions, it is apparent that the shock-standoff distances, the boundary-layer heights, and the boundary-layer shapes are in agreement, even though slight differences in boundary-layer height are noticed. The boundary layers found by Esfahanian (1991) appear to be slightly thicker than those found using the current method. This is thought to be due to the slightly different free-stream conditions used by the researchers. Esfahanian (1991) uses a free-stream Reynolds number of 3.1×10^5. The current research uses a free-stream Reynolds number of 3.3×10^5. Given the subsequent agreement of the LST results, this discrepancy is not thought to be terribly important. The graphical agreement of all of these comparisons with the results reported by Esfahanian (1991) and Stetson et al. (1984), as well as the demonstrated grid-independence, gives the confidence needed to proceed with the LST study.

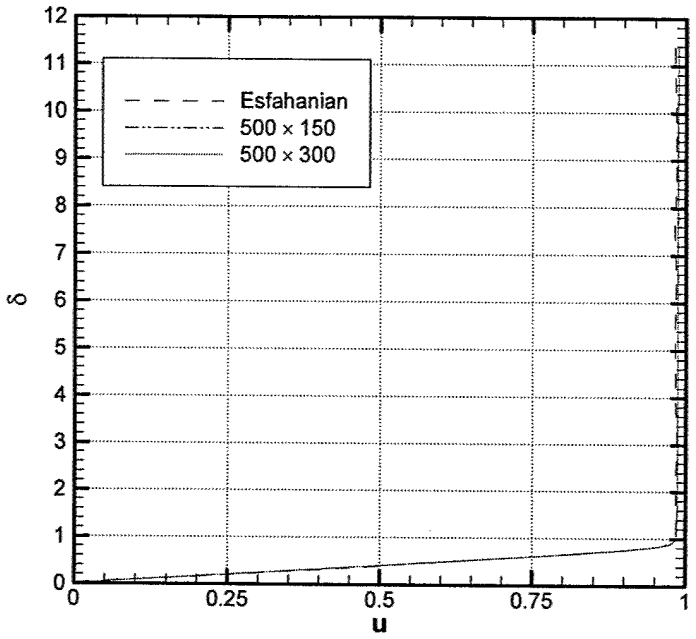

Figure 6: Comparison of streamwise velocity profiles at s = 175, Stetson case.

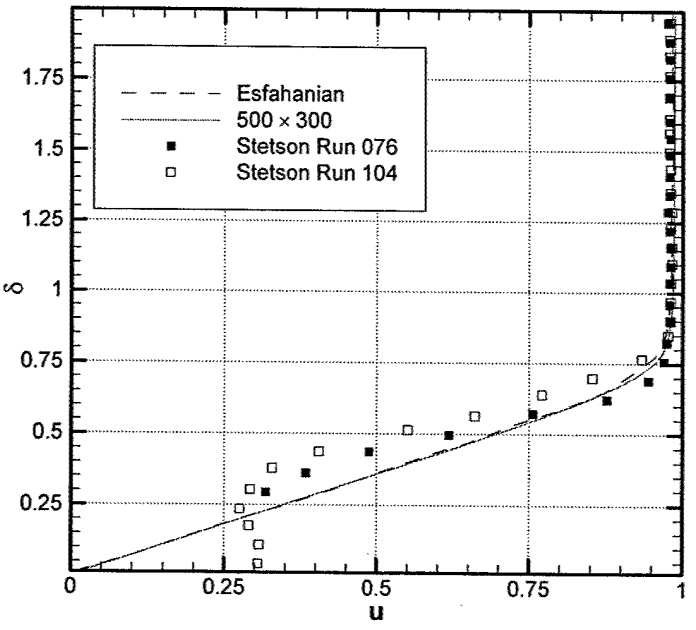

Figure 7: Comparison of streamwise velocity profiles at s = 128, Stetson case.

Wall-Temperature Distribution The traditional approach for numerically investigating the Stetson et al. (1984) case is to model the cone-wall as being adiabatic. This is the standard boundary-condition used by numerical investigators, and was the intent of the Stetson experiment. As Schneider (2001b) points out, this assumption is not supported by the experimental evidence. However, because this boundary condition is "standard" it provides an opportunity to make useful comparisons with other numerical results, as well as an opportunity to quantify the difference made by using a more physically-appropriate boundary condition.

As shown in Figure 8, the computed adiabatic wall temperature distribution is higher than the experimentally measured temperature distributions. Schneider further observes that, as consecutive experimental runs are made, the measured temperature distribution rises from run to run, until an equilibrium temperature distribution is reached. Schneider hypothesizes that the heat capacity of the model prevents the wall temperature from reaching the adiabatic value.

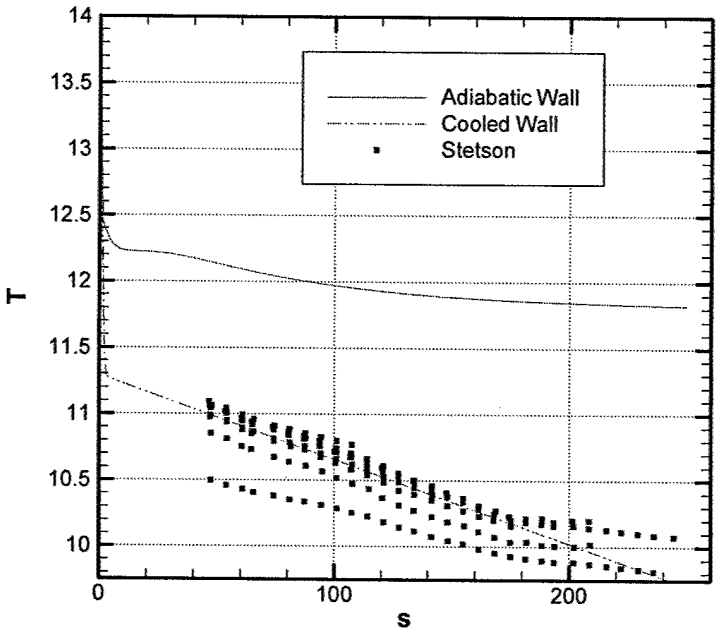

Figure 8: Comparison of wall-temperatures using different methods, Stetson case.

An investigation is proposed, whereby the modeled wall temperature would approach the adiabatic value near the nose (where the model's heat capacity is less), and approach the experimentally determined distribution farther down the cone's surface. This is accomplished by joining a parabola (at the nose) to a line (at the rear). This function is then approximated by a composite function, with continuous derivatives, which would be more suitable for modeling purposes. This distribution is shown in Figure 8. Contrasting the adiabatic-wall boundary condition and the cooled-wall condition, there are expected to be differences in the boundary-layer profiles. Such differences are important because of the well-known behavior of the second mode - that it is tuned to the height of the boundary layer. The wavelength of the most-amplified

frequency is roughly equal to twice the boundary-layer height. Accordingly, the frequency of the most-amplified wave can be estimated using the edge-velocity and the estimated-wavelength. All else being equal, as the boundary-layer height increases, one expects the most-amplified second-mode frequency to decrease. Keeping in mind that as *s* increases, the boundary-layer height also increases, one observes this frequency-decreasing behavior in Stetson's experimental results shown in Figure 2.

Consider the effect of cooling the boundary layer by cooling the wall. For air, the viscosity decreases with decreasing temperature. Thus, one expects that by cooling the wall, the boundary layer would become thinner. This expectation is confirmed by examining the temperature profiles compared in Figure 9. The cooled-wall boundary layers at s = 175 are roughly 15% thinner than their counterparts for the adiabatic wall. Thus, one expects the most-amplified frequency to be slightly larger for the cooled-wall case.

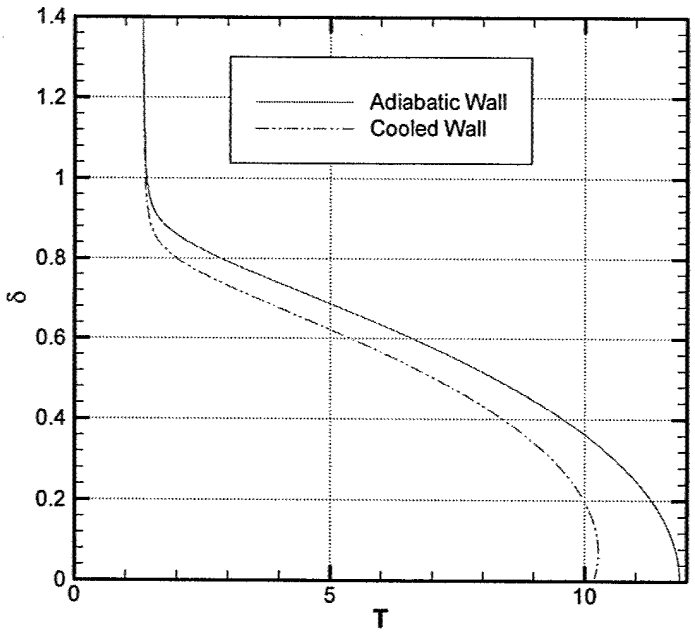

Figure 9: Temperature profiles at s=175, different wall-temperature models, Stetson case.

Linear-Stability Results

Verification The grid-independence of the LST solutions is demonstrated in Table 3 by comparing the calculated wavenumbers for the series of different grid sizes.

Grid	α	Norm. Dev. (α)	Norm. Dev. (α_i)
500 × 150	2.81743 + -0.0524956 *i*	-	-
1000 × 150	2.81737 + -0.0524988 *i*	2.13×10^{-5}	6.09×10^{-5}
500 × 300	2.81542+ -0.0538071 *i*	8.51×10^{-4}	2.50×10^{-2}

Table 3: Comparison for wavenumbers at $\omega = 2.60$, s = 175, Stetson case.

Many researchers who use numerical methods use Stetson et al. (1984) as a means for comparison of their growth rates with the experimentally determined growth rates and other researchers' numerically determined growth rates. Some of the numerical investigations of the Stetson case include Malik et al. (1990), Esfahanian (1991), Kufner et al. (1993), Rosenbloom et al. (1999), and Zhong and Ma (2002).

In this report, comparisons are made with the experimental results of Stetson et al. (1984). Comparisons are also made with the numerical results of Malik et al. (1990), who use a Parabolized Navier-Stokes (PNS) approach, and with the numerical results of Esfahanian (1991), who uses a Thin-Layer (TNLS) approach. Further comparisons are made with the results of Rosenbloom et al. (1999). All of the numerical results use a linear-stability formulation to determine the growth or decay of disturbances.

It has become a de-facto standard to make comparisons of growth rates at the location on the cone that corresponds to $s = 175$. This provides a convenient reference for numerical researchers; however, comparisons between numerical results and the experimental results of Stetson et al. (1984) are problematic. Although there is generally good agreement among different researchers' numerical results, linear-stability theory appears to over-predict the experimentally determined growth rates by roughly 60%.

There have been a variety of theories to try to explain this discrepancy. Schneider (2001b) points out that Stetson postulates that non-linearities are present at station 175, visible in Figure 7b in Stetson et al. (1984). It has been pointed-out that the wall temperature at $s = 175$ is not adiabatic, whereas the numerical (basic-state) models assume an adiabatic wall; this effect is investigated in this report. Mack (1987) points out that the origin of the disturbances (receptivity) is not addressed by linear-stability theory - nor by the experiment. Furthermore, Mack (1987) points out that the experimentally determined growth rates are found using the y-locations that have the peak wide-band response - not with regard to the location of the peak of an individual frequency component. New experimental initiatives, led by Schneider et al. (2002) and Maslov (2001), address these issues. These efforts also are discussed in this report.

Figure 3 shows a comparison of the growth rates, found as functions of frequency at $s = 175$, with the results of Stetson et al. (1984), Esfahanian (1991), and Malik et al. (1990). The present

results are in general agreement with the other numerical results, and show the classical disagreement with the experimental results. These verifications provide the necessary confidence to make further investigations of the Stetson et al. (1984) case, and to consider the recent experimental investigations of Maslov (2001).

Wall-Temperature Distribution As discussed earlier, comparison of second-mode growth rates at $s = 175$ has become the de-facto standard among computational investigations. The growth rates found using the cooled-wall boundary condition are compared with the adiabatic-wall growth-rates, and other results, in Figure 3. As expected, the most-amplified frequency for the cooled-wall case is slightly higher than the most-amplified frequency for the adiabatic-wall case. Also, the peak growth-rate for the cooled-wall case is slightly higher than the peak growth-rate for the adiabatic-wall case.

Using a more physically appropriate wall-temperature boundary-condition does not by itself bridge the apparent disjoint between the numerical and experimental growth-rates.

N-Factor Investigation Continuing the suggestion of Schneider (2001b), comparisons are made of integrated growth-rates among the computations and the experiments. This may be a more appropriate comparison because the experiments measure the disturbance amplitudes, then calculate the growth-rates based on the change in disturbance amplitudes. The integrated growth-rates, N-factors, depend on the two integration-endpoints s_0 and s_1, and are calculated as follows.

$$N = \ln\left(\frac{A_1}{A_0}\right) = \int_{s_0}^{s_1} -\alpha_i \, ds \tag{8}$$

To place the current results in the context of the Stetson experiment, the adiabatic-wall, cooled-wall, Rosenbloom, and Stetson N-factors are compared, using $s = 195$ as the reference location; these are shown in Figure 4 and Figure 10. With respect to Rosenbloom's results, the current adiabatic-wall results appear to provide better agreement with the experimental results. Furthermore, the cooled-wall results appear to be in better experimental-agreement than the adiabatic-wall results. The current results' agreement with the experimental results is best in the range of frequencies $2.4 < \omega < 2.8$. Examining the experimentally determined amplitudes from Figure 2, this frequency range corresponds with those frequencies that are most-amplified in the experiment.

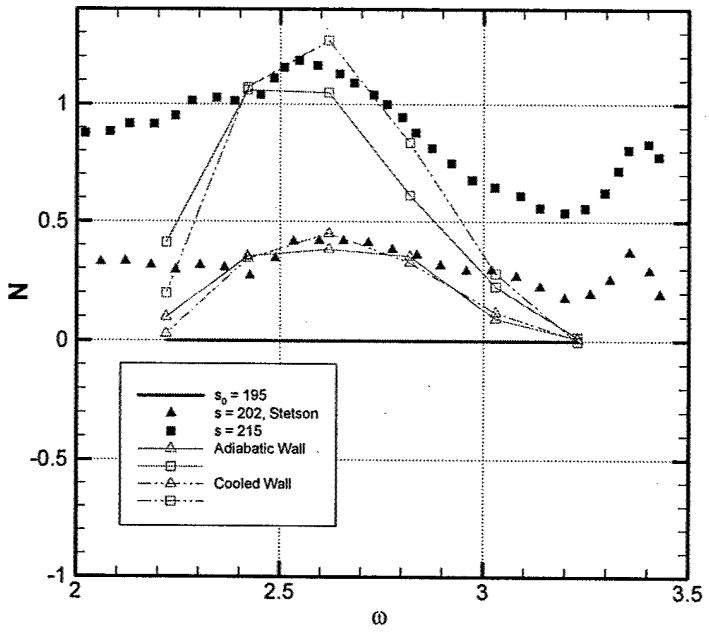

Figure 10: Comparison of N-factors, s_0=195, Stetson case.

The N-factor curves for a series of individual disturbance waves are considered, using s = 195 as the reference location. It is surmised that if a discernible linear-growth region exists, the extent of such a region can be identified by choosing $s_0 = 195$. For example, the results for $\omega = 2.62$ are shown in Figure 11, demonstrating the existence of a linear-growth region. The traditional under-prediction of growth-rates at s = 175 might also be explained by examining Figure 11.

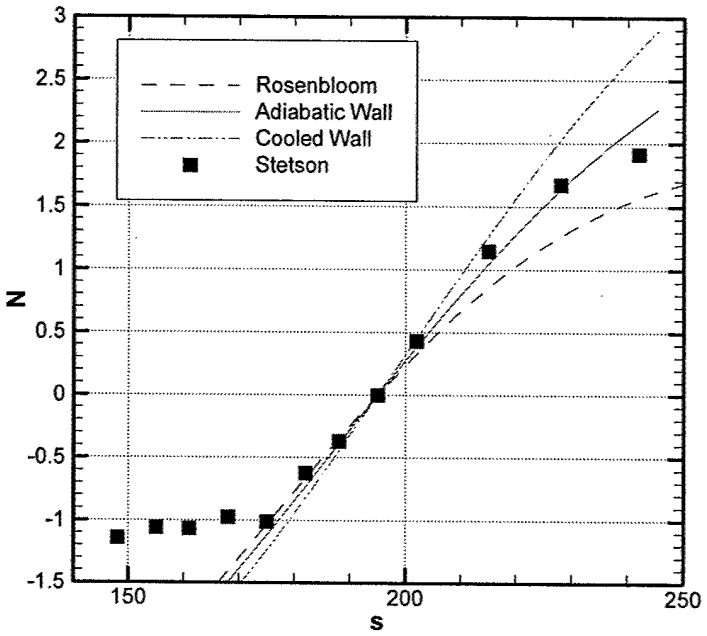

Figure 11: N-factor comparison, ω=2.62, Stetson case.

It is proposed that linear-stability theory describes the growth of second-mode disturbances for $2.4 < \omega < 2.8$, and for the region $195 < s < 215$. The frequencies in this range correspond to the most-amplified second-mode frequencies. Upstream of $s = 195$, it is postulated that the amplified second-mode waves have not yet fully distinguished themselves from the noise. Indeed, the experimental N-factor curves suggest that the experimental-numerical disjoint at $s = 175$ may be attributed to signal-noise problems, rather than to non-linearity. For locations downstream of $s = 215$, perhaps non-linear interactions are important – behavior that cannot be captured using LST. Also, the agreement between the experiment and the current predictions appears better for the computations that use an experimentally determined wall-temperature distribution.

3.1.4 Maslov Case

The renewed interest in fundamental boundary-layer stability mechanisms includes two ongoing experimental efforts; one is at Purdue University, the other is at the Institute of Theoretical and Applied Mechanics (ITAM) at Novosibirsk, Russia. The goal of this set of programs is to conduct two independent experiments, using the same freestream conditions and the same geometries (Maslov 2001). The two experimental teams choose to fix their respective freestream flows at Mach 6, so that the second mode instability is dominant, yet the stagnation temperature is low enough that the cost and effort required to realize the flow conditions remains feasible (Schneider et al. 2002).

According to Maslov (2001), the ITAM facility is notable for the long run times possible at high-enthalpy conditions. Run times can be as long as 30 minutes, allowing the surface of the

experimental models to approach the adiabatic temperature for the conditions. In terms of noise (unintended disturbance state) within the flow, the ITAM facility is a conventional tunnel. The Purdue facility is known as a quiet tunnel because extraordinary steps are taken to minimize noise in the flow, as summarized by Schneider et al. (2002). The noise levels found in conventional wind tunnels can be an order of magnitude larger than those found in flight. Such changes in the disturbance environment can change the nature of the relevant instability mechanisms (Schneider 2001a). Thus, the motivation for minimizing the noise environment at the Purdue facility is to allow measurements in ground-test facilities to be more reliable predictors of flight performance (Schneider et al. 2002). As both efforts progress, one of the interesting results will be to compare how the boundary-layer stability responses change according to the different freestream disturbance environments.

Experimental results reported by Maslov (2001) are compared, in this report, with the numerical basic-state and LST results generated using the methods described herein. In this section, the authors paraphrase from the description of the experiment provided by Maslov (2001). The experimental model is a 7° half-angle, right-circular cone, with a nose radius of 0.75 mm and a length of 500 mm. Roughly twenty separate experimental runs are made to gather all the data. In the experiment, artificial disturbances are generated using a high-frequency glow-discharge system. Thermal disturbances are introduced by a single 0.5 mm orifice through the surface of the cone, at a distance of 69 mm ($s = 92.0$) from the nose. Pressure transducers and thermocouples are used to measure the surface pressure and temperature, respectively. The local mass-flow, $1/2\,\rho\sqrt{u^2+v^2}$, is measured using a hot-wire anemometer system. This hot-wire system is controlled by a three-component traverse system that provides a positional accuracy of 0.01 mm. The hot-wire system is used to provide mass-flow measurements for both the basic-state and the disturbance-state.

Computational Parameters

The freestream conditions used for the numerical simulation: $M_\infty = 6.00$, $p_{t\infty} = 1.00$ MPa, $T_{t\infty} = 383$ K, are used as a first-order representation of the twenty experimental runs. The conditions used for the computation are summarized in Table 4. The ideal-gas model is used, with Pr = 0.72. The resulting freestream Reynolds number (based on nose radius) is Re_r = 9807. The computation extends to $s = 400$. The frequency of the experimental disturbance-state is 275 kHz. For the stability calculations, to convert from the dimensional frequency to the non-dimensional frequency, note that for $f^* = 275$ kHz, $\omega = 1.57$. It is also noted that for all the calculations presented in this chapter, only two-dimensional waves are considered – $\beta = 0$.

Variable	Normalization	Value
s, δ	r^*	7.500×10^{-4} m
ρ	ρ_∞^*	4.705×10^{-2} kg/m^3
u	U_∞^*	8.237×10^{2} m/s
p	p_∞^*	6.333×10^{2} Pa
T	T_∞^*	4.670×10^{1} K
ω	U_∞^* / r^*	1.098×10^{6} rad./s
α	$1/r^*$	1.333×10^{3} rad./m

Table 4: Non-dimensionalizations used for Maslov case.

Basic-State Results

Verification Three cases are run using the flow conditions described in Table 4. The mesh sizes used are 500 × 150, 1000 × 150, and 500 × 300. The truncation error in the solution is estimated by calculating the normalized deviation for a series of values such as wall-temperature. The location s = 325 is chosen to be a reference because, as discussed later, it falls within what is postulated to be a region of linear growth. As such, it is an interesting place to make comparisons. Surface temperatures are compared at s = 325, as well as the normalized deviations, are shown in Table 5, showing convergence of $O(10^{-4})$.

Grid	Temperature	Normalized Deviation
500 × 150	7.116721	-
1000 × 150	7.116741	2.81×10^{-6}
500 × 300	7.116481	3.37×10^{-5}

Table 5: Comparison for surface temperature at s = 325, Maslov case.

Comparison with Experiment A surface-temperature comparison is made in Figure 12. Maslov shows a comparison with his team's calculated surface-temperatures for laminar and turbulent boundary-layers, which is also shown in Figure 12. Maslov cites the temperature rise along the surface of the cone as evidence of laminar-turbulent transition. For Figure 12, it is also

notable that the surface-temperatures found experimentally are not in good agreement with those found numerically. Further discussion and investigation are needed to resolve this discrepancy.

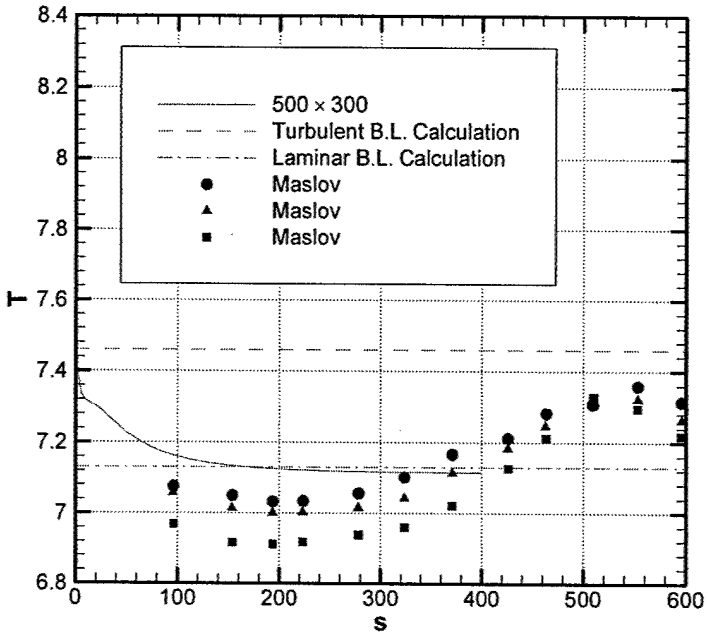

Figure 12: Comparison of wall-temperatures, Maslov case.

In the experiment, hot-wire anemometry is used to measure the mass-flow perpendicular to the length of the wire. Mass-flow profiles are compared at $s = 181$ and $s = 221$, in Figure 13. There is non-negligible disagreement between the numerical and experimental results. In these (and other) comparisons, the numerically determined boundary-layers are consistently thinner than the experimentally measured boundary layers. These comparisons are made over the range $143 < s < 303$. Despite the disagreement in boundary-layer heights, the mass-flow values in the inviscid region, for all these figures, agree within the experimental scatter.

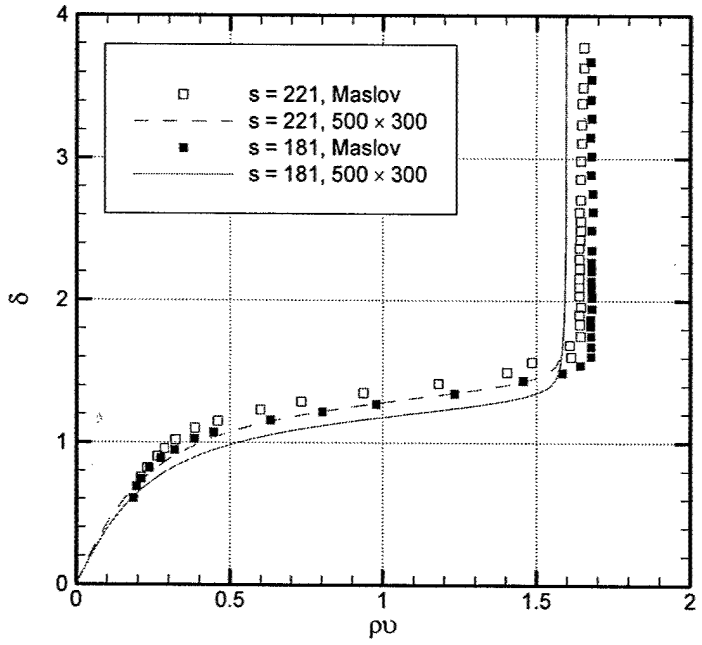

Figure 13: Comparison of mass-flow profiles, Maslov case.

Linear-Stability Results

Verification The truncation error in the LST solution is estimated by calculating the normalized deviation for the calculated wavenumber. As with the basic-state solution, the location $s = 325$ is chosen to be a reference. Wavenumbers are compared at $s = 325$, as well as the normalized deviations, are shown in Table 6, showing convergence of $O(10^{-2})$.

Grid	α	Norm. Dev. (α)	Norm. Dev. (α_i)
500 × 150	1.74162 + 0.0279057 *i*	-	-
1000 × 150	1.74162 + 0.0279041 *i*	9.17×10^{-7}	5.73×10^{-5}
500 × 300	1.74119 + 0.0280217 *i*	8.81×10^{-4}	4.46×10^{-3}

Table 6: Comparison for wavenumbers at $\omega = 1.57$, s = 325, Maslov case.

Comparison with Experiments As a part of the Maslov experiment, a glow-discharge system is used to introduce a point-source disturbance on the surface of the cone, at a frequency of 275 kHz ($\omega = 1.57$). This frequency is chosen by the experimental team because, using naturally occurring disturbances, the largest-amplitude second-mode response is observed at this frequency.

Hot-wire anemometry is used to measure the 275 kHz-response within the boundary-layer at a series of surface locations. Using the information from the boundary-layer responses, Maslov

(2001) catalogues the amplitudes and phases of the second-mode disturbances in mass-flow. Maslov (2001) observes that the two-dimensional waves are the most unstable, agreeing with theory and previous experimental observation. Additionally, the team estimates that the boundary-layer begins its transition to turbulence at s ≈ 450. This estimate is supported by the surface-temperature data shown in Figure 12.

Thus, the phase of a given disturbance can be defined using a series of locally determined wavenumbers. The procedure for phase calculation is very similar to that used for the N-factor calculation.

$$\phi(s) = \phi_0 + \int_{s_0}^{s} \alpha_r \, ds \tag{9}$$

Phase angle as a function of surface distance is also determined experimentally, as shown in Figure 14. The phase of the numerically determined disturbance is determined as described above, fixing s_0 such that the phases match at $s = 324$.

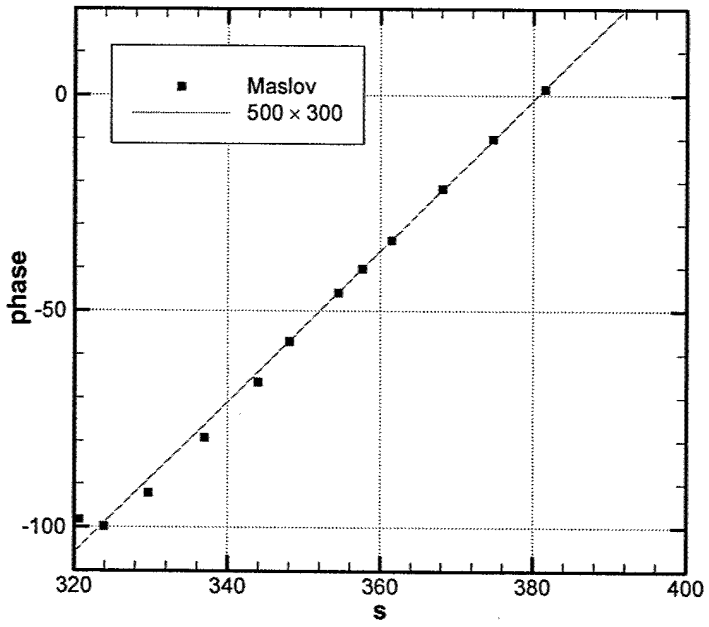

Figure 14: Disturbance-phase comparison for second-mode wave at ω = 1.57, Maslov case.

Maslov (2001) is unable to determine, with confidence, the phases upstream of this point due to the low disturbance-amplitudes. Downstream of $s = 324$, however, there is excellent agreement between the numerically and experimentally determined phase angles. This helps to verify that the same physical disturbance is being "seen" in both studies.

Further comparison of amplitude-profiles and phase-profiles of a 2D-disturbance in mass-flow, at $s = 381$, is shown in Figure 15. Both sets of amplitudes are scaled such that their maximum

amplitudes are unity. The numerically and experimentally determined amplitudes are in reasonably good agreement, considering the differences in boundary-layer height noted for the basic-state comparisons. It should also be noted that this comparison is made at a location (s = *381*) where non-linear behavior is suspected. This is the only location for which Maslov (2001) provides both amplitude and phase profiles for a disturbance.

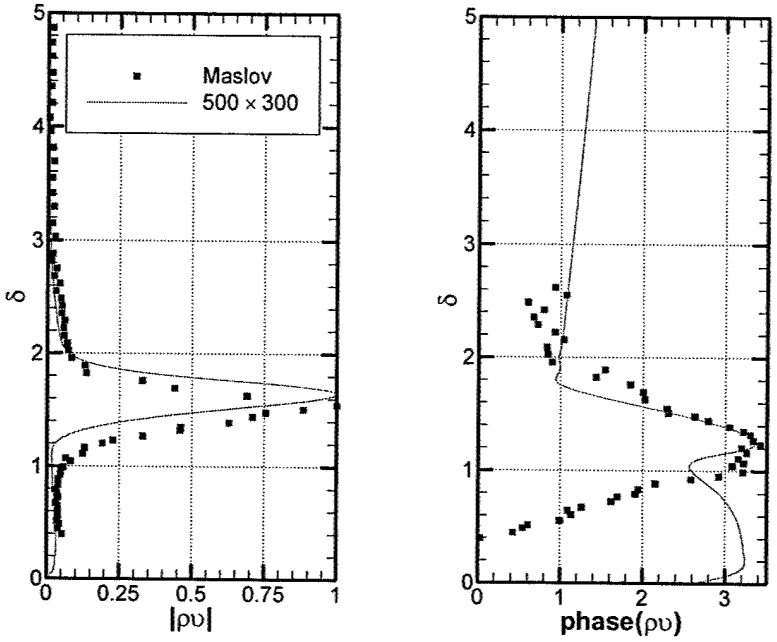

Figure 15: Amplitude- and phase-profiles for mass-flow, ω = 1.57, s = 381, Maslov case.

Maslov (2001) determines the relative growth of the amplitudes of disturbances at 275 kHz. These relative amplitudes are converted into N-factors using s_0 = *300*. Although the choice for s_0 is arbitrary, the reason for its choice can be seen in Figure 16. The experimentally- and numerically-determined N-factors are compared, postulating that a linear-growth region begins near s = *300*. There is reasonably good agreement among the experimental and numerical amplifications in the region *300* < s < *350*. Downstream of this, it is suggested that the discrepancy between linear-stability theory and the experimental results is due to non-linear amplification. The discrepancy upstream of s = *300* requires further discussion and investigation.

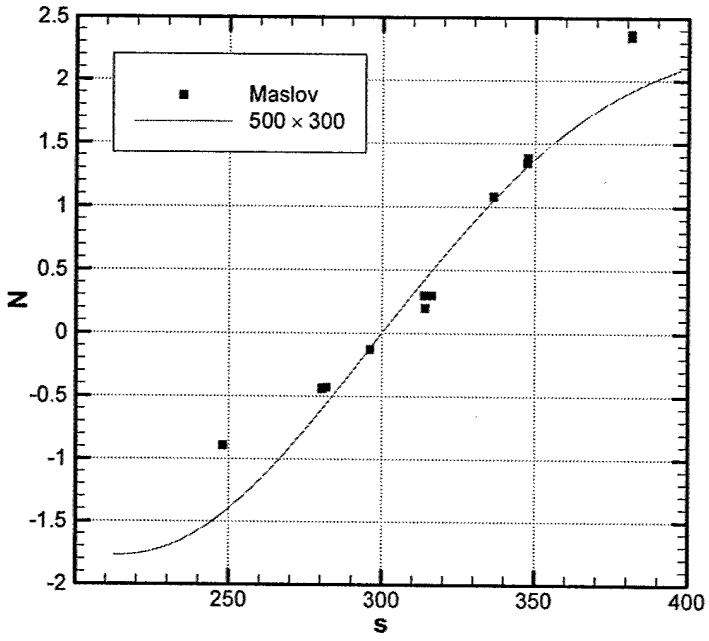

Figure 16: Comparison of second-mode N-factors at ω = 1.57, Maslov case.

3.2 Nonequilibrium Chemistry

Regarding the investigation of more energetic flows as would be found in flight, we have used the numerical methods described above and modelled a 27 degree half angle, 20 cm long, 2.54-cm nose radius untapered, axisymmetric cone. The purpose is qualitative comparison with Johnson & Candler at Mach 13.6 and 20 km altitude who studied a similar geometry but tapered and including windows. We considered a 5-species nonequilibrium-chemistry model: N2, O2, NO, N, O. Figure 17a shows our temperature predictions and Figure 17b shows those of Johnson & Candler. Again the comparisons are very good, lending confidence to our formulations.

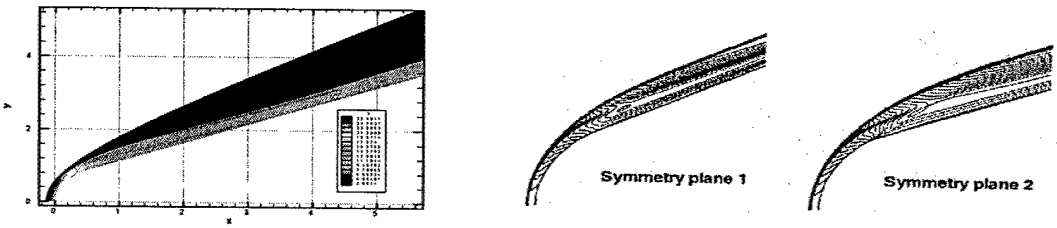

Figure 17: Comparison of basic state with that of Johnson & Candler.

Stability calculations are being finalized and will be reported in a future publication.

3.3 Hyper2000 fore-body

For our work on the Hyper2000 forebody, we anticipated that the compression ramps complicate the problem and developed an adaptive-grid scheme based on the SIERRA method (Laflin & McRae) to capture the details in the corners. The disturbance to the shock wave results in a shock-wave line that is hard to estimate ahead of time and thus it is very difficult to use a shock-fitting method. To develop the basic-state code, we first examined a simpler 2D 2.5-degree-half-angle blunt nose with a 5.5-degree compression corner at x=2.2. Even though the corner is farther upstream, this test case is representative of the Hyper2000.

The SIERRA weight function, developed by Laflin & McRae, is easy to compute and promotes both grid-node clustering and grid-alignment adaptation. Before application to the complicated Hyper2000 geometry, we verified the algorithm for a 2D, 7-degree-half-angle blunt nose without any corners. Then Figure 18a shows the adapted grid for the compression-corner geometry. Figure 18b shows the density contour to be qualitatively compared with a density contour in the vicinity of the corner from Balakumar (Figure 18c, AIAA 2002-2848).

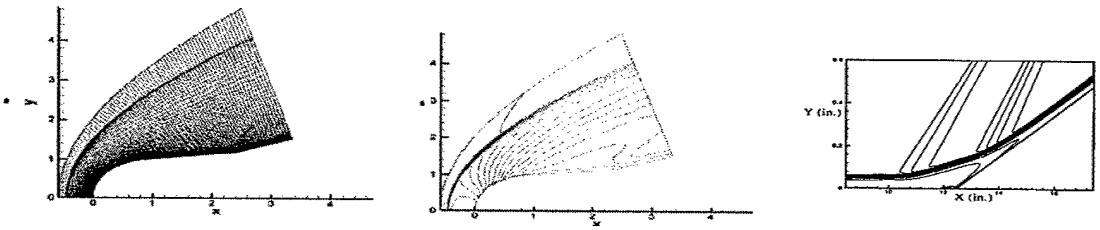

Figures 18a through 18c

Figure 19a shows computed streamlines in the vicinity of the corner again for qualitative comparison with Balakumar's results (Figure 19b). The comparisons are very good.

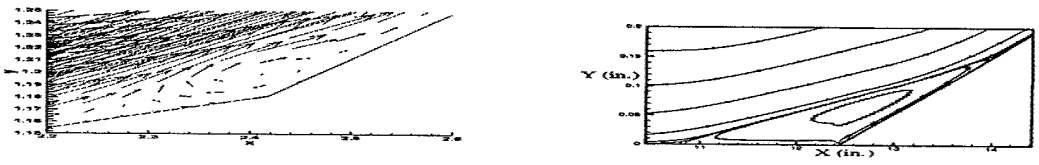

Figure 19.

Next we solve the flow field for the compression corner situated further downstream using a shock-capturing method (Figures 20 and 21). We now have a problem with computational memory since the number of grid points required is very large. In addition, we have tried using the industry-standard COBALT flow solver to compute the flow field of the Hyper2000 geometry (2 compression corners). Figure 22 shows the grid, and figure 23 shows the density contours. Still there is a problem with insufficient computer resources, we cannot apply enough grid points.

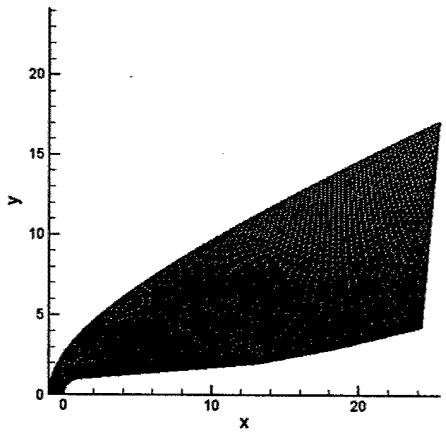

Figure 20: Shock-cap grid for nose with a compression corner at x=13

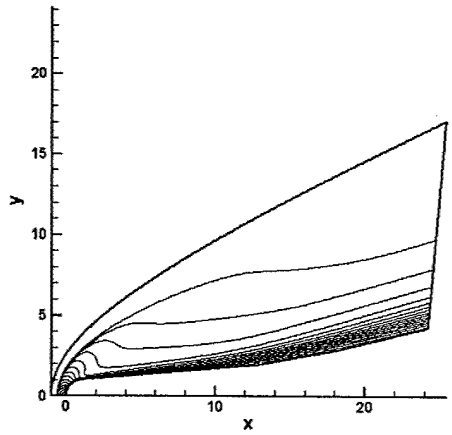

Figure 21: Flow velocity contour

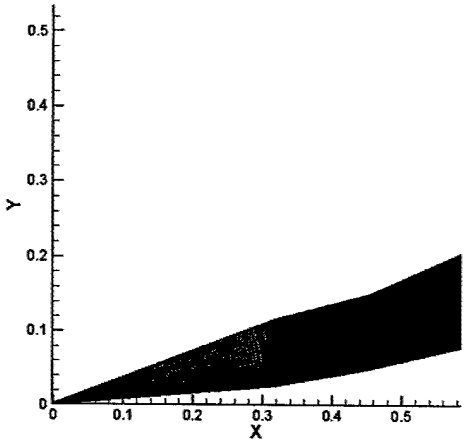

Figure 22: COBALT grid for Hyper2000

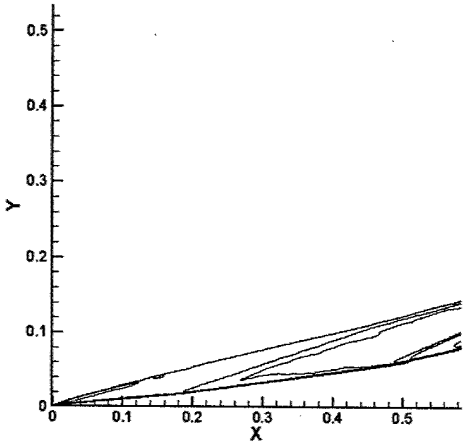

Figure 23: COBALT density contour

This necessitates dividing the region into several domains and computing in parallel to accurately model the Hyper2000 geometry. To verify our methods, we chose a simple geometry, namely a 7° half angle blunt nose without a compression corner. Figure 25 shows velocity contours from parallel computations of three regions as shown in figure 24. The procedure is to calculate the flow properties in the first region using downstream boundary conditions determined from interior conditions. Then using results of the first region as upstream conditions, we calculate the flow properties in the second region, and so forth for any number of regions in parallel. Then we go back to the first region and iterate until convergence. The method adapts to multiple processors – each region is assigned to a processor – and Message-Passing-Interface (MPI) is used to exchange information between the processors.

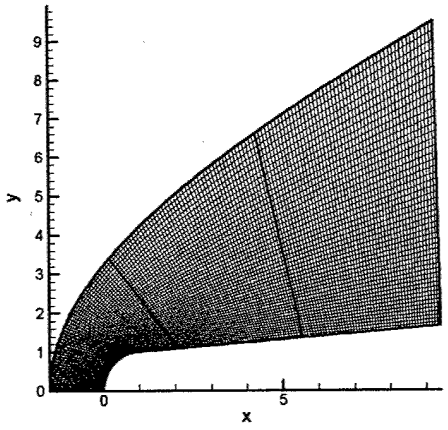

Figure 24: Three regions in parallel

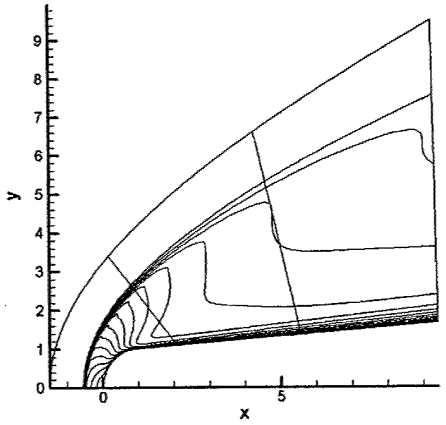

Figure 25: Flow velocity contour

Next we demonstrate the same method for a 7° half angle blunt nose with a corner using five regions as shown in figure 26. Figure 27 shows well converged velocity contours for the geometry.

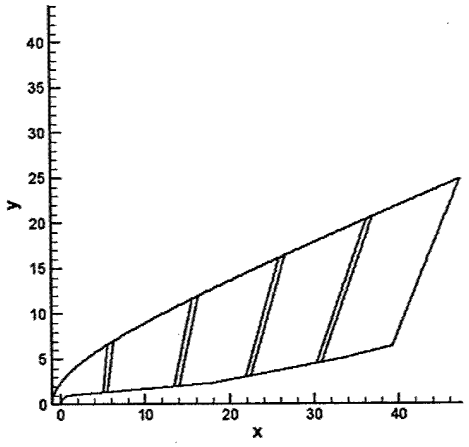

Figure 26: Five regions boundary
(nose with a corner at x=18)

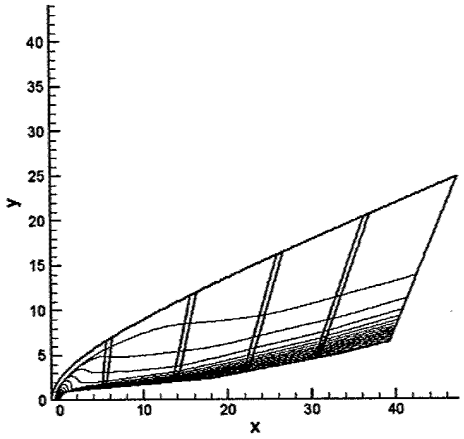

Figure 27: Flow velocity contour

Once basic-state results are finalized, stability calculations on the second mode will be completed for the Hyper2000 forebody using our existing verified codes.

4 Current Status and Future Plans

Work on the computation of hypersonic laminar-turbulent transition continues unfunded. Collaborations with Maslov will continue. Ian Lyttle's PhD dissertation involving the round cone and nonequilibrium chemistry will be completed in May 2003. The basic state (both ideal gas and non-equilibrium chemistry) is completed and stability calculations are underway. Yasutoshi Asada's PhD dissertation involving the Hyper 2000 forebody will be completed in May 2004. The basic state is nearly finalized and stability calculations will be underway shortly using our existing verified codes. Prof. Reed attended the LASTRAC Workshop at NASA Langley in November 2002 on the use of the linear stability theory/nonlinear parabolized stability equation code LASTRAC (Langley Stability and Transition Code) – this tool is well developed and validated and will also be used to complete the present research on second-mode instabilities.

The computational work has direct application to the DARPA QSP program; Prof. Reed is working to develop the distributed roughness laminar flow control concept in coordination with Prof. William Saric at Arizona State University. The program involves a supersonic wind-tunnel test at ASU, a flight test on an F-15B out of NASA Dryden, and a flight-Reynolds-number test in the Unitary Plan Wind Tunnel at NASA Langley. Close coordination with the airframers also under contract is a key element of the QSP program.

References

Balakumar, P., H. Zhao, and H. Atkins. 2002. Stability of hypersonic boundary layers over a compression corner, AIAA 2002-2848.

Demetriades, A. 1977. Laminar boundary layer stability measurements at Mach 7 including wall temperature effects. Tech. Rep. 77-1311, AFOSR.

Eiseman, P.R. 1987. Adaptive grid generation. Computer Methods in Applied Mechanics and Engineering, Vol. 64, No. 1-3, pp.321-376, October.

Esfahanian, V. 1991. *Computation and Stability Analysis of Laminar Flow over a Blunt Cone in Hypersonic Flow*. Ph.D. diss., The Ohio State University.

Federov, A., A. Shiplyuk, A. Maslov, E. Burov, and N. Malmuth. 2003. Stabilization of high speed boundary layer using a porous coating. *AIAA Paper No. 03-1270.*

Hudson, M. L., N. Chokani, and G. V. Candler. 1997. Linear stability of hypersonic flow in thermochemical nonequilibrium. *AIAA Journal 35(6):958.*

Kendall, J. M. 1975. Wind tunnel experiments relating to supersonic and hypersonic boundary-layer transition. *AIAA Journal* 13(3):290–299.

Kimmel, R. L. 2003. Aspects of hypersonic boundary-layer control. *AIAA Paper No. 03-0772.*

Kufner, E., U. Dallmann, and J. Stilla. 1993. Instability of hypersonic flow past blunt cones – effects of mean flow properties. *AIAA Paper No. 93-2983.*

Laflin, K.R. and D.S. McRae. 1996. Solution-dependent grid-quality assessment and enhancement, 5th International Conference on Numerical Grid Generation in Computational Field Simulations, April 1-5.

Laflin, K.R. and D.S. McRae. 1996. Three-dimensional dynamic viscous flow computations using near-optimal grid redistribution algorithm, Proceedings, First AFOSR Conference on Dynamic Motion CFD, Rutgers Univ., New Brunswick, NJ, June 2-5.

Laflin, K.R. 1997. Solver-independent r-refinement adaptation for dynamic numerical simulations, Ph.D Dissertation, Department of Mechanical and Aerospace Engineering, N.C. State University, Raleigh, NC.

Lehoucq, R., D. Sorensen, and C. Yang. 1998. *ARPACK Users' Guide: Solution of Large-Scale Eigenvalue Problems with Implicitly Restarted Arnoldi Methods.* SIAM.

Mack, L. M. 1984. Boundary-layer stability theory. Tech. Rep. 709, AGARD.

Mack, L. M. 1987. Stability of axisymmetric boundary layers on sharp cones at hypersonic speed. *AIAA Paper No. 87-1413.*

Malik, M. R., R. E. Spall, and C.-L. Chang. 1990. Effect of nose bluntness on boundary layer stability and transition. *AIAA Paper No. 90-0112.*

Maslov, A. 2001. Experimental study of stability and transition of hypersonic boundary layer around blunted cone. Tech. Rep. 1863-2000, Institute of Theoretical and Applied Mechanics.

Message Passing Interface Forum. 1995. MPI: A message-passing interface standard. Tech. rep., University of Tennessee.

Rosenbloom, I., S. Hein, and U. Dallmann. 1999. Influence of nose bluntness on boundary-layer instabilities in hypersonic cone flows. *AIAA Paper No. 99-3591.*

Schneider, S. P. 2001a. Effects of high-speed tunnel noise on laminar-turbulent transition. *Journal of Spacecraft and Rockets* 38(3).

Schneider, S. P. 2001b. Hypersonic laminar instability on round cones near zero angle of attack. *AIAA Paper No. 01-0206.*

Schneider, S. P., S. Matsumara, S. Rufner, C. Skoch, and E. Swanson. 2002. Progress in the operation of the Boeing/AFOSR Mach-6 Quiet Tunnel. *AIAA Paper No. 02-3033.*

Stetson, K., E. Thompson, J. Donaldson, and L. Siler. 1984. Laminar boundary layer stability experiments on a cone at Mach 8, Part 2: Blunt cone. *AIAA Paper No. 84-0006.*

Wright, M., G. Candler, and M. Prampolini. 1996. Lower-upper relaxation method for the Navier-Stokes equations. *AIAA Journal* 34(7).

Zhong, X. and Y. Ma. 2002. Receptivity and linear stability of Stetson's Mach 8 blunt cone stability experiments. *AIAA Paper No. 02-2849.*